



## The low-frequency flattening of the radio spectrum of giant H II regions in M 101

Downloaded from: <https://research.chalmers.se>, 2025-05-21 15:38 UTC

Citation for the original published paper (version of record):

Gajovic, L., Heesen, V., Brüggén, M. et al (2025). The low-frequency flattening of the radio spectrum of giant H II regions in M 101. *Astronomy and Astrophysics*, 695.  
<http://dx.doi.org/10.1051/0004-6361/202453003>

N.B. When citing this work, cite the original published paper.

# The low-frequency flattening of the radio spectrum of giant H II regions in M 101

L. Gajović<sup>1,\*</sup>, V. Heesen<sup>1</sup>, M. Brüggén<sup>1</sup>, H. W. Edler<sup>2,1</sup>, B. Adebahr<sup>3,2</sup>, T. Pasini<sup>4</sup>, F. de Gasperin<sup>4</sup>,  
A. Basu<sup>5,6</sup>, M. Weżgowiec<sup>7</sup>, C. Horellou<sup>8</sup>, D. J. Bomans<sup>2</sup>, H. Dénes<sup>9</sup>, and D. Vohl<sup>10,2</sup>

<sup>1</sup> Hamburger Sternwarte, University of Hamburg, Gojenbergsweg 112, 21029 Hamburg, Germany

<sup>2</sup> ASTRON, Netherlands Institute for Radio Astronomy, Oude Hoogeveensedijk 4, Dwingeloo 7991 PD, The Netherlands

<sup>3</sup> Ruhr University Bochum, Faculty of Physics and Astronomy, Astronomical Institute (AIRUB), Universitätsstrasse 150, 44801 Bochum, Germany

<sup>4</sup> INAF – Istituto di Radioastronomia, Via P. Gobetti 101, 40129 Bologna, Italy

<sup>5</sup> Thüringer Landessternwarte, Sternwarte 5, 07778 Tautenburg, Germany

<sup>6</sup> Max-Planck-Institut für Radioastronomie, Auf dem Hügel 69, 53121 Bonn, Germany

<sup>7</sup> Obserwatorium Astronomiczne Uniwersytetu Jagiellońskiego, ul. Orła 171, 30-244 Kraków, Poland

<sup>8</sup> Chalmers University of Technology, Onsala Space Observatory, SE-43992 Onsala, Sweden

<sup>9</sup> School of Physical Sciences and Nanotechnology, Yachay Tech University, Hacienda San José S/N, 100119 Urcuquí, Ecuador

<sup>10</sup> Anton Pannekoek Institute for Astronomy at the University of Amsterdam, University of Amsterdam, P.O. Box 94249, 1090 GE Amsterdam, The Netherlands

Received 14 November 2024 / Accepted 6 February 2025

## ABSTRACT

**Context.** In galaxies, the flattening of the spectrum at low radio frequencies below 300 MHz has been the subject of some debate. A turnover at low frequencies could be caused by multiple physical processes, which can yield new insights into the properties of the ionised gas in the interstellar medium.

**Aims.** We investigate the existence and nature of the low-frequency turnover in the H II regions of M 101.

**Methods.** We study the nearby galaxy M 101 using the LOw Frequency ARray (LOFAR) at frequencies of 54 and 144 MHz, Aperitif at 1370 MHz, and published combined map from the Very Large Array (VLA) and Effelsberg telescope at 4850 MHz.

**Results.** The spectral index between 54 and 144 MHz is inverted at the centres of H II regions. We find a significant low-frequency flattening at the centres of five out of six H II regions that we selected for this study.

**Conclusions.** The low frequency flattening in H II regions of M 101 can be explained with two different free-free absorption models. The flattening is localised in a region smaller than 1.5 kpc and can only be detected with high resolution (better than 45"). The detection of low frequency flattening has important consequences for using radio continuum observations below 100 MHz to measure extinction-free star-formation rates.

**Key words.** radiation mechanisms: general – H II regions – galaxies: ISM – galaxies: individual: M 101 – radio continuum: galaxies

## 1. Introduction

Non-thermal (synchrotron) and thermal (free-free) radiation processes play a key role in the radio continuum emission of nearby galaxies. Synchrotron radiation in galaxies is produced by cosmic-ray (CR) electrons that spiral around magnetic field lines and free-free radiation by free electrons scattering off ions (e.g. Niklas et al. 1997; Basu et al. 2012; Tabatabaei et al. 2017). The synchrotron radiation dominates the spectrum at radio frequencies below a few GHz. CRs that produce synchrotron radiation originate from regions with higher star formation in spiral galaxies because they are accelerated through shocks during supernova explosions (Green 2014; Caprioli et al. 2010). The spectrum of synchrotron radiation is a power law  $S_\nu \propto \nu^\alpha$ , with a radio spectral index  $\alpha$  between  $-1.2$  and  $-0.5$  for nearby galaxies (e.g. Gioia et al. 1982; Li et al. 2016; Tabatabaei et al. 2017). At higher frequencies (around 10 GHz), the contribution of thermal free-free emission from ionised

gas with the spectral index  $\alpha = -0.1$  becomes significant and the spectrum should flatten out (e.g. Tabatabaei et al. 2017; Klein et al. 2018). Lower-frequency (below 100 MHz) observations at high spatial resolution only recently became possible with the advent of digital interferometers, such as the LOw Frequency ARray (LOFAR; van Haarlem et al. 2013), and sophisticated calibration strategies (van Weeren et al. 2016; Tasse et al. 2018; de Gasperin et al. 2019). Still, the spectral behaviour in this frequency regime remains largely unexplored, but there is evidence that the spectrum of nearby galaxies flattens or even turns over below 100 MHz.

The low frequency flattening was first noticed in statistical studies of galaxy samples. Israel & Mahoney (1990) observed that the radio intensities at 57.5 MHz are systematically lower than the values extrapolated from higher frequency measurements assuming a power law spectrum. They reported a dependence of the flattening on the inclination of the galaxies and attributed it to free-free absorption. However, Hummel (1991) was unable to find any correlation using the same data and stressed that a steepening of the spectrum at high frequencies due

\* Corresponding author; lovorka.gajovic@uni-hamburg.de

to propagation effects of the relativistic electrons is equally plausible. A more recent study by [Chyży et al. \(2018\)](#), using additional data at 150 MHz, confirms the results of [Hummel \(1991\)](#).

An alternative explanation for the low frequency flattening was provided by [Pohl & Schlickeiser \(1990\)](#) and [Pohl et al. \(1991a,b\)](#) who modelled the energy spectra of CR electrons that experience simultaneous injection, diffusion, convection, adiabatic deceleration, as well as radiative and ionisation losses. Observing a large sample of 250 bright galaxies at three pairs of frequencies with the lowest being 74 and 325 MHz, [Marvil et al. \(2015\)](#) reports a curvature in the mean spectrum with a magnitude of approximately  $\Delta\alpha = -0.2$  per logarithmic frequency decade. They propose two reasons for this effect: free–free absorption at low frequencies or a curved synchrotron spectrum resulting from curvature in the underlying energy distribution of CR electrons.

To observe the low-frequency spectral flattening in individual galaxies it is usually necessary to look at exceptional targets where the flattening is significant at comparatively high frequencies. In the centre of the Milky Way, thermal absorption shapes the spectra below 500 MHz ([Roy & Pramesh Rao 2006](#)). Meanwhile, the integrated spectrum of the Milky Way has a detectable turnover at about 3 MHz ([Brown 1973](#)). In the starburst galaxy M 82, turnovers were detected in the global integrated radio spectrum ([Klein et al. 1988](#)), the core regions ([Adebahr et al. 2013](#)), and individual sources near the galactic centre ([Adebahr et al. 2017](#)). There is also a low frequency turnover in the integrated spectrum of the starburst galaxy NGC 253 ([Marvil et al. 2015](#)). The ultra-luminous infrared galaxy Arp 220 shows a turnover in the central region at around 1 GHz ([Varenius et al. 2016](#)) and in the integrated spectrum ([Anantharamaiah et al. 2000](#)).

More recently, [Ramírez-Olivencia et al. \(2022\)](#) investigate the luminous infrared galaxy Arp 299 using sub-arcsecond LOFAR observations at 150 MHz. In order to fit the SED in the nucleus of this galaxy, they use two models for the free–free absorbing and emitting thermal gas. In the first model the gas is smooth and continuous medium while in the second model it is distributed in a clumpy fashion ([Lacki 2014](#); [Conway et al. 2018](#)). They find that both models fit their data reasonably well. While the smooth continuous model can explain the SED by an injection of relativistic electrons subjected to synchrotron, bremsstrahlung, and ionisation losses, the clumpy model yields negligible losses but a more realistic thermal fractions.

In the dwarf galaxy IC 10, spectra of several compact H II regions were measured down to 320 MHz ([Basu et al. 2017](#)). These spectra show evidence of thermal free–free absorption at low frequencies. A region of the edge-on galaxy NGC 4631 observed by [Stein et al. \(2023\)](#) is found to have a very flat radio spectrum with a flattening at low-frequencies. Local spectral turnovers are also observed in jellyfish galaxies, where they might be due to ionisation losses in compressed gas ([Lal et al. 2022](#); [Ignesti et al. 2022](#); [Roberts et al. 2024](#)). The only average spiral galaxy where the low frequency effects were studied in detail is M 51 ([Gajović et al. 2024](#)). Using high-resolution low-frequency radio maps, they show that the flattening spatially correlates with the neutral HI gas in the galaxy which points to CR ionisation losses as an important mechanism aside from free–free absorption.

In summary, there is still no consensus about what causes the low-frequency flattening at radio frequencies below 300 MHz and whether there is a turnover. The most commonly suggested explanation for the flattening is free–free absorption. However, ionisation losses, CR ageing, or synchrotron-self absorption

**Table 1.** Basic properties of M 101.

Name	M 101
Alternative names	NGC 5457
RA (J2000)	14 <sup>h</sup> 03 <sup>m</sup> 12 <sup>s</sup> .5
Dec (J2000)	+54°20′56″
Morphology	SAB(rs)cd <sup>(a)</sup>
Apparent size	40′ <sup>(b)</sup>
Distance	6.644 ± 0.087 Mpc <sup>(c)</sup>
Position angle	36° <sup>(d)</sup>
Inclination angle	26° <sup>(d)</sup>
Scaling	1″ ↔ 32.21 pc

**Notes.** <sup>(a)</sup>[de Vaucouleurs et al. \(1991\)](#) <sup>(b)</sup>[Vorontsov-Vel’ Yaminov & Arkhipova \(1962\)](#) <sup>(c)</sup>[Hiramatsu et al. \(2023\)](#) <sup>(d)</sup>[Hu et al. \(2018\)](#).

could also be responsible. The physical mechanism most likely depends on the galaxy’s environment and is possibly a combination of multiple effects. We therefore choose to explore the low frequency spectrum of the nearby spiral galaxy M 101 that is known to have multiple giant H II regions in a diffuse disc. While the previous study of M 51 surprisingly shows no correlation with ionised gas ([Gajović et al. 2024](#)), this may be because the H II regions are embedded in strong background radiation and thus are hard to study individually. Therefore, we focus on the giant H II regions in M 101 that are very massive and luminous, so they can be studied in the radio continuum ([Israel et al. 1975](#)).

The galaxy M 101 (details in Table 1) and its H II regions have already been studied at radio frequencies down to 610 MHz ([Israel et al. 1975](#); [Graeve et al. 1990](#); [Berkhuijsen et al. 2016](#)). It is possible to observe M 101 at a high spatial resolution because of its large angular diameter of 40′ and a distance of only 6.6 Mpc. [Israel et al. \(1975\)](#) mapped M 101 at 610 MHz with 1′ resolution, and specifically noted the brightest H II regions and how the structure visible in radio compares to two different H $\alpha$  maps. [Graeve et al. \(1990\)](#) studied the H II region spectra and found them to be flat due to thermal emission. However, they did not observe a turnover because their measurements did not extend to frequencies below 610 MHz. In this work, we use LOFAR to observe M 101 at frequencies of 54 and 144 MHz with a resolution higher than 26″ and search for the low frequency flattening in the H II regions.

This paper is structured as follows: in Sect. 2 we present the data from LOFAR, Apertif and literature. Sect. 3 describes the data preparation, including the selection of the H II regions. In Sect. 4 we present our results that are discussed in Sect. 5. Finally, we conclude in Sect. 6.

## 2. Data

We used four radio maps at frequencies of 54, 144, 1370 and 4850 MHz at resolutions between 11″ and 30″. The details of each map are presented in Table 2 and in the following sections.

### 2.1. LOFAR LBA observations

M 101 was observed with the LOFAR Low-Band Antenna (LBA) system at a central frequency of 54 MHz and in a bandwidth of 24 MHz as part of the LOFAR LBA Sky Survey (LoLSS; [de Gasperin et al. 2021, 2023](#)). The galaxy is covered by three survey pointings (P209+55, P210+52, P214+55) with a primary beam response of at least 30% and each pointing was

**Table 2.** Observation parameters for the radio maps used in the analysis.

Telescope (Survey)	Central frequency [MHz]	Beam size	Beam position angle PA [°]	Original $\sigma$ rms noise [ $\mu\text{Jy beam}^{-1}$ ]	Convolved regridded $\sigma_c$ rms noise [ $\mu\text{Jy beam}^{-1}$ ]	Flux density scale uncertainty $\epsilon_r$ [%]	Ref.
LOFAR (LoLSS)	54	26'5" $\times$ 14'7"	114.8	1700	1700	10	1
LOFAR (LoTSS)	144	20'0" $\times$ 20'0"	/	130	170	10	2
Apertif	1370	15'1" $\times$ 11'0"	1.4	20	30	5	3
VLA + Effelsberg	4850	30'0" $\times$ 30'0"	/	59	59	5	4

**Notes.** (1) Observed by [de Gasperin et al. \(2021\)](#), reprocessed in this paper; (2) [Shimwell et al. \(2022\)](#); (3) This work; (4) [Weżgowiec et al. \(2022\)](#).

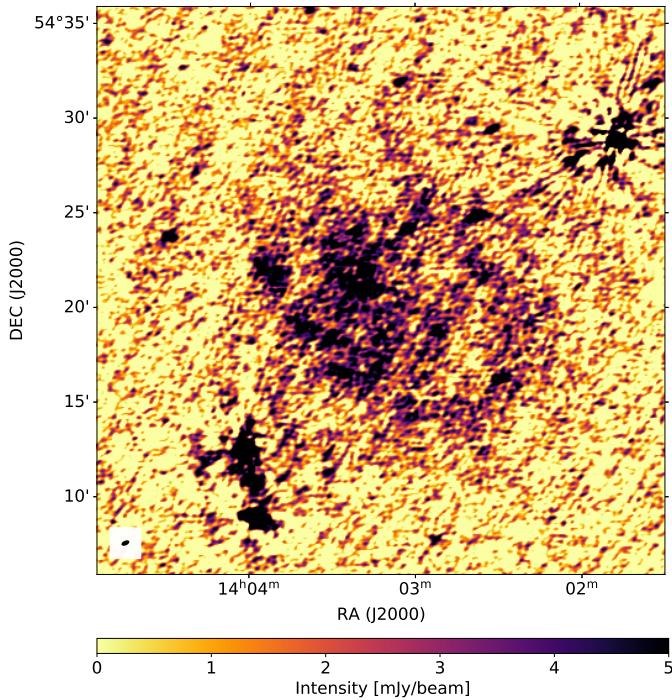


**Fig. 1.** Radio map of M 101 at 54 MHz observed with LOFAR LBA. The beam size is shown with the black ellipse in the bottom left corner.

observed for 8 h. The observations were calibrated for direction-independent ([de Gasperin et al. 2021](#)) and direction-dependent effects ([de Gasperin et al. 2023](#)). To further process the pointings, for each observation we subtracted all sources except for a circular region with 0.25° radius around M 101 from the visibility data using the source models and calibration solutions found in the direction-dependent calibration carried out as part of LoLSS. We then phase-shifted the measurement sets of the individual observations and pointings to the location of M 101 and corrected them for the primary beam response in the new phase centre. We also applied the direction-dependent calibration solutions of the nearest direction-dependent calibrator source from LoLSS (for more details about the calibration procedure see e.g. [Pasini et al. 2022](#)). All nine observations were then imaged together to allow for a deep deconvolution of the extended emission associated with M 101. The LOFAR LBA radio map of M 101 at 54 MHz is presented in Fig. 1 and the main parameters of the map are in Table 2.

## 2.2. Apertif observations

The Apertif system is a Phased Array Feed (PAF) receiver operating at a central frequency of 1.4 GHz with a bandwidth of 300 MHz mounted on the dishes of the Westerbork Synthesis Radio Telescope (WSRT). The PAF allows simultaneous observations of 40 individual compound beams covering an area of 6.6 deg<sup>2</sup>.

We inspected the Apertif Wide and Medium Deep Extragalactic Survey (AWES/AMES; [Adams et al. 2020](#)) observations and the Apertif archive for coverage of M 101. Fortunately, the galaxy is situated very close to the intrahour-variable source J1402+5347 ([Oosterloo et al. 2020](#)) that was observed twelve times during the Apertif operational phase. We considered a compound beam response level of 10% as useful for imaging. This resulted in three compound beams (numbers 29, 35 and 36) of each observation being considered for further inspection.

For the data reduction, we used the cross-calibrated visibilities provided by the `apercal`-pipeline averaged down to 192 channels for every compound beam data set. These data were then directionally dependent self-calibrated and finally imaged in total power using the advanced Apertif reduction pipeline ([Kutkin et al. 2023](#)).

We found that eight out of the twelve observations had sufficient data quality in terms of dynamic range and resolution to be usable for our analysis. The corresponding observation ids are 190807041, 190913045, 191010041, 191102001, 191207034, 200106009, 200128124 and 200302074. The final image was generated by convolving all 24 images (one per beam and observation) to the largest common synthesised beam and correcting by their appropriate primary beam model ([Dénes et al. 2022](#)). The final Apertif radio map at 1370 MHz is presented in Fig. 2 and the main parameters of the map are in Table 2.

## 2.3. Other radio continuum data

The observation of M 101 at 144 MHz was done with the LOFAR high-band antennas (HBA) as a part of the LOFAR Two-metre Sky Survey data release 2 (LoTSS-DR2; [Shimwell et al. 2022](#)). The map of M 101 used in this work was reprocessed by [Heesen et al. \(2022\)](#) along with 44 other nearby galaxies. They compared the low 20'' and the high 6'' resolution maps and made sure that the integrated flux density matches. We used the low resolution map because it is more sensitive to diffuse emission and the maps at other frequencies have similar beam sizes, so this map did not have to be convolved to a significantly larger beam. We also consulted the high resolution map to identify background sources. The flux density scale error of LoTSS-DR2 is below 10% ([Shimwell et al. 2022](#)), which is the value we

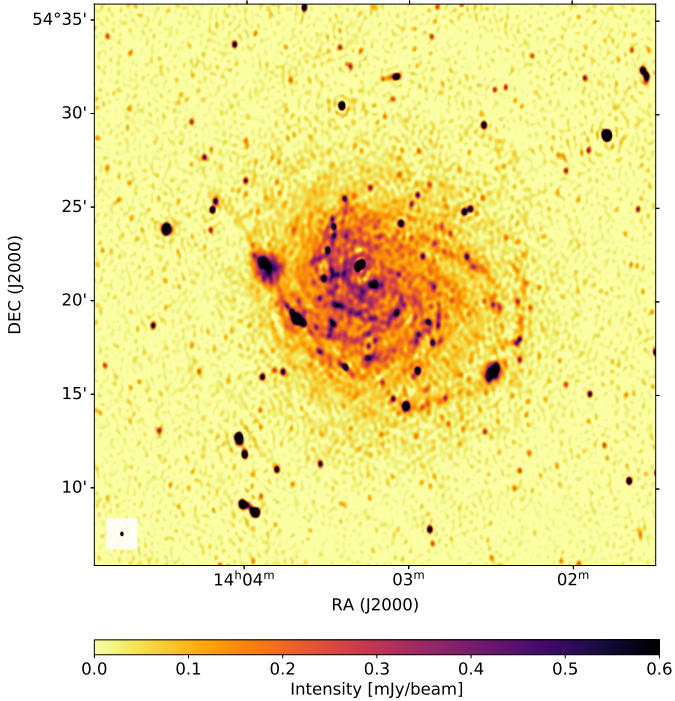


**Fig. 2.** Radio map of M 101 at 1370 MHz observed with Apertif. The beam size is shown with the black ellipse in the bottom left corner.

adopted. The main parameters of the LOFAR HBA radio map are presented in Table 2.

The radio map of M 101 at 4850 MHz is a combination of VLA and Effelsberg maps presented by Weżgowiec et al. (2022). Because of the large angular size of M 101, the VLA observations include multiple pointings separated in two observation projects (19B-027 and 15B-292). The results of Effelsberg observations were previously published by Berkhuijsen et al. (2016). The combination of the two data sets restores the large-scale diffuse emission that cannot be recovered if the short baselines are not sufficiently covered by the interferometer. More details on the VLA calibration and the combination of data sets are presented in Weżgowiec et al. (2022). In this work, we used only the total intensity map and assumed a flux density scale uncertainty of 5%, which is standard for the VLA (Konar et al. 2013). The main parameters of the combined VLA and Effelsberg radio map are presented in Table 2.

### 3. Data preparation

The radio maps were additionally processed in the following way. All data, except for the 4850 MHz, were convolved to the largest common beam of  $26.52'' \times 20''$  with the position angle  $PA = 115^\circ$ . For the convolution, we used the routine CONVOL of the software package MIRIAD (Sault et al. 1995). The 4850 MHz data were kept with the original  $30''$  beam and for flux density measurements we made sure to take into account the different beam size for that map. We did not convolve to the largest common beam of all data (which would be  $30''$ ) because that would make the large rms noise in the LBA map even worse. The rms error dominates over the flux scale error in small regions that we study, so it was important to keep it as small as possible.

All maps were then aligned to a common world coordinate system, re-gridded to a pixel size of  $2''$ , as well as transformed into the reference pixel and image size. We used the world coor-

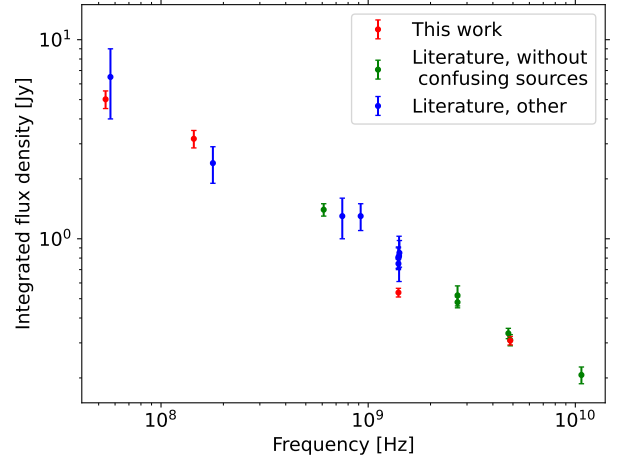


**Fig. 3.** Integrated spectrum of M 101. The flux density measurements from the maps used in this work (red) compared to literature flux density measurement, separated into those where bright background sources surrounding the galaxy are excluded (green) and are not excluded (blue).

dinate system of the  $H\alpha$  map by Hoopes et al. (2001) as the reference. This was achieved using the REGRID routine of MIRIAD.

The rms noise  $\sigma$  of each individual image was determined by calculating the standard deviation over an emission-free area. The total noise was calculated as a combination of the rms noise and the flux density scale uncertainty (both listed in Table 2).

#### 3.1. Data validation

We first checked if the integrated flux density of M 101 in our maps matches the literature measurements. We prepared a mask to calculate the integrated flux density in our maps, which includes all the emission from the galaxy, but excludes nearby bright radio sources (e.g. NVSS J140147+542852 and NVSS J140357+540852). We specifically made sure we include the H II region NGC 5471, which is located outside the galactic disc to the east. We did not remove the background sources in cases where their emission overlapped with the disc of the galaxy (e.g. NVSS J140318+542159). The mask is shown in Appendix A.

We compile the integrated flux density of M 101 from the literature and from the maps used in this paper in Appendix B. We also note the type of telescope used for the observation, the beam size and most importantly whether the bright background sources around the galaxy are included in the flux density measurements. We show these measurements in Fig. 3. The data points roughly follow a power-law. We do not see a significant flattening of the integrated spectrum at low frequencies. Comparing our data with the literature, we notice that there might be missing large-scale flux density in the 1370 MHz Apertif map. The inclusion of background sources cannot account for this difference. For this reason, the Apertif map was not used for studying the galaxy as a whole, only the compact H II regions that are less likely to be affected by missing flux density issue.

We additionally checked if our maps are reliable to study spectra in smaller regions. In Fig. 4, we plot the spectra of four background radio sources surrounding M 101. The spectra are well-fit by a power-law between 54 MHz and 5 GHz, and the offset of the data points is minimal. Because the small scale flux is reliable, we can continue with analysing the spectra of H II regions in M 101. We used the Apertif map for studying the

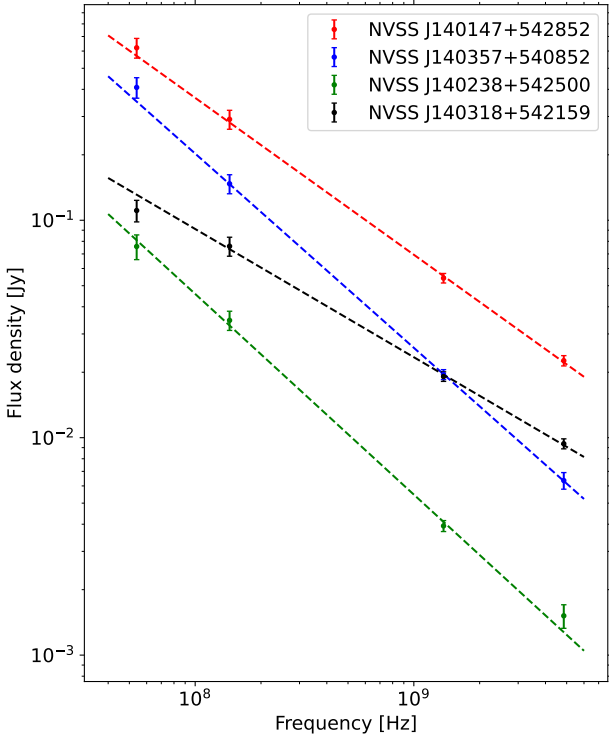


**Fig. 4.** Spectra of four selected background sources. The spectra follows a power law as expected confirming that there are no flux density problems in our images at small scales.

spectra of smaller regions that are not affected by the missing large-scale flux density.

### 3.2. H II region selection

More than a thousand H II regions were identified in M 101 (Hodge et al. 1990), but we want to focus on the prominent giant H II regions. There is no consensus in literature on what constitutes a giant H II region, but they generally have a large physical size and they are very bright at both optical and radio frequencies. Therefore, we combine the most comprehensive lists of giant H II regions in M 101 (Skillman & Israel 1988; Hippelein 1986; Dodorico et al. 1983) with coordinate positions (Gordon et al. 2008) in Table 3.

For this paper, we selected the H II regions that are prominent at low radio frequencies, specifically in the 144 MHz map. We chose the 144 MHz map because the frequency is high enough to not be affected by low frequency flattening. Additionally, the 144 MHz map has a good signal-to-noise ratio. In this selection, we used the H $\alpha$  map by Hoopes et al. (2001) to define the H II region boundaries. First, we manually plotted circles that include all the H $\alpha$  emission from the H II region and mostly exclude the surrounding emission. Second, we refined the H II region boundary by selecting everything above  $10\sigma$  in the H $\alpha$  image. In Fig. 5, the H II region boundaries defined from H $\alpha$  are plotted on top of the 144 MHz map. Regions 0–5 show a clear excess of emission compared to the disc surrounding them. For regions 0–5, surface brightness is higher than 7 mJy/beam while for the other regions it is lower than 5 mJy/beam. We chose these six regions (the galactic centre, NGC 5447, NGC 5455, NGC 5461, NGC 5462, and NGC 5471) for the spectral analysis in this work. Coincidentally, those are the same regions selected for analysis

**Table 3.** Coordinates of H II regions considered for analysis. Regions 0–5 were selected.

No.	Name	RA(J2000)	Dec(J2000)	Ref.
0	Centre	14:03:12.48	+54:20:55.4	1
1	NGC 5447	14:02:28.18	+54:16:26.3	1,2,3,4
2	NGC 5455	14:03:01.13	+54:14:28.7	1,2,3,4
3	NGC 5461	14:03:41.36	+54:19:04.9	1,2,3,4
4	NGC 5462	14:03:53.19	+54:22:06.3	1,2,4
5	NGC 5471	14:04:29.35	+54:23:46.4	1,2,3,4
6	NGC 5449	14:02:26.0	+54:19:48.0	2,5
7	Hodge 1013 <sup>(a), (b)</sup>	14:03:31.0	+54:21:14.5	1,2,4,6
8	Searle 5	14:02:55.05	+54:22:26.6	1,2
9	Searle 12	14:04:11.11	+54:25:17.8	1,2,4
10	Hodge 67 <sup>(a)</sup>	14:02:19.92	+54:19:56.4	1
11	Hodge 70/71 <sup>(a)</sup>	14:02:20.50	+54:17:46.0	1
12	Hodge 681 <sup>(a)</sup>	14:03:13.64	+54:35:43.0	1

**Notes.** (1) Gordon et al. (2008); (2) Hippelein (1986); (3) Skillman & Israel (1988); (4) Dodorico et al. (1983); (5) Corwin (1995); (6) Hodge et al. (1990). <sup>(a)</sup>Identification numbers according to Hodge et al. (1990). <sup>(b)</sup>Also called Hodge 40, according to Hodge (1969).

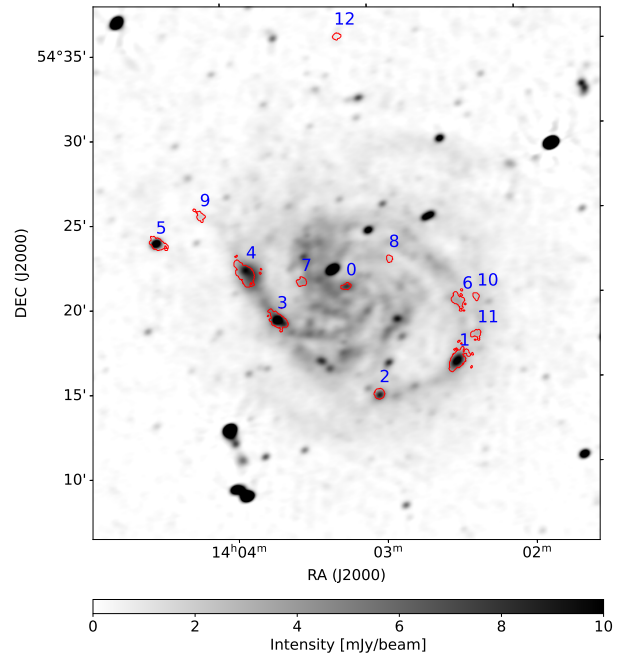


**Fig. 5.** H II region boundaries determined from H $\alpha$  (Hoopes et al. 2001) plotted on top of 144 MHz radio map. The region boundaries are red and the blue numbers correspond to their identification numbers in Table 3. For the analysis we select or only regions 0–5, which are bright at 144 MHz. Note that these boundaries were only used in the H II region selection.

by Israel et al. (1975), likely because of their brightness at radio frequencies.

## 4. Results

### 4.1. Spectral index maps between 54 and 144 MHz

We calculated the radio spectral index of M 101 between 54 and 144 MHz. Both radio maps were convolved to the same beam ( $26.52'' \times 20''$  beam with PA =  $115^\circ$ ) and re-gridded to the same

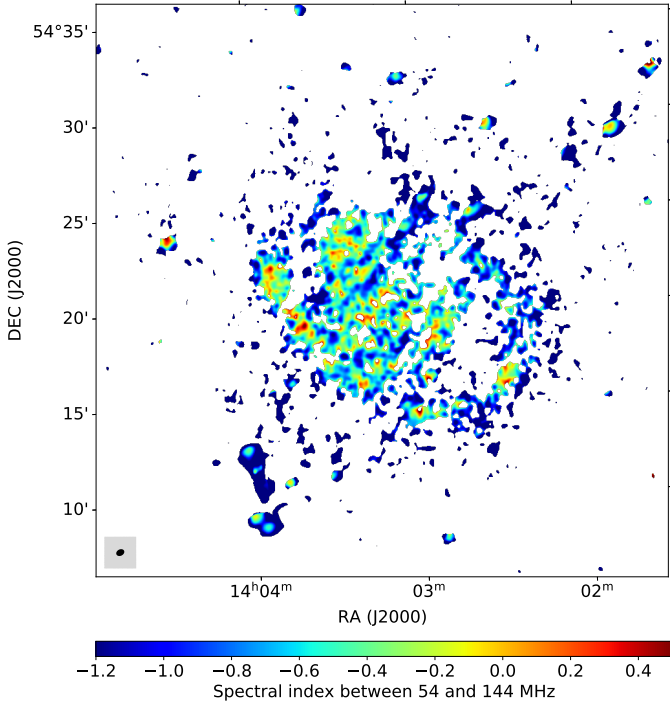


**Fig. 6.** Spectral index map of M 101 between 54 and 144 MHz. White areas below  $2\sigma$  are excluded. The beam size is shown with the black ellipse in the bottom left corner.

coordinate grid. The spectral indices were calculated in a standard way by taking the logarithmic ratio of the flux densities in two maps over the logarithmic frequency ratio. The errors in the spectral index maps were calculated by propagating the errors from the individual maps, which are a combination of the flux density scale uncertainty and the rms noise measured away from the source (both listed in Table 2). The regions below  $2\sigma$  (in either map) were excluded from the analysis. We chose a  $2\sigma$  exclusion limit instead of the usually used  $3\sigma$  because otherwise the high noise in the LBA map would significantly limit the area in which the spectral index is calculated. We also note that LOFAR has good coverage of short baselines which correspond to large angular scales on the sky. We can therefore trust that the LOFAR maps are not missing large scale emission from M 101 and the spectral indices presented here are reliable.

The index of M 101 between 54 and 144 MHz is shown in Fig. 6 and the corresponding error map can be found in Appendix C. Significant areas of flat or inverted spectra index are present, especially at the positions of the H II regions.

In Fig. 7 we present cutouts of the spectral index maps focused on the six H II regions that we selected for this study. For the majority of the regions we see a small area of positive spectral index right at the centre of several H II regions. There, we expect the highest free-free absorption because of high density of ionised gas. If we want to observe the turnover in the spectrum, we should focus on these very central areas.

#### 4.2. SEDs of H II regions and fits

In the spectral index cutouts (Fig. 7) we see that there are areas of positive spectral index at the very centre of H II regions (except NGC 5447). For this reason we measure the spectra in circular areas with increasing size starting from the largest beam size ( $30''$ ) up to twice the beam size ( $60''$ ) with a  $10''$  step. These

areas are centred on the position of the H II region according to Gordon et al. (2008), which are listed in Table 3. Alternative centres could be defined directly from H $\alpha$  data, but the position would not change more than the size of our beam and an alternative definition would not affect our results significantly. Here, we include measurements at all four frequencies (54, 144, 1370, and 4850 MHz) because the flux densities in small regions are accurate in all the maps, which we confirm by checking the spectra of background sources in Sect 3.1.

The spectra are shown in Fig. 8 with different lines indicating different areas within which the fluxes are measured. We can clearly see a deviation from a power law with decreasing area, or increasing resolution. We initially model the spectra using a synchrotron power law with an internal free-free absorbing medium. We make an assumption that in the H II region the absorbing thermal plasma coexists with the synchrotron-emitting CR electrons. Thus, the model assumes a thoroughly mixed medium of thermal gas and cosmic rays. This “internal” model includes emission and free-free absorption internal to a continuous synchrotron-emitting region. As Kapińska et al. (2017), the model only considers the non-thermal synchrotron emission and the free-free absorption of that emission. At such low frequencies, the free-free emission is insignificant compared to the synchrotron emission so the free-free self-absorption is neglected and free-free absorption only affects synchrotron emission. Modelling the radio spectrum with a synchrotron power law with an internal free-free absorbing screen, the flux density  $S_\nu$  depends on frequency as (Tingay & de Kool 2003):

$$S_\nu = S_0 \left( \frac{\nu}{\nu_0} \right)^\eta \left( \frac{1 - e^{-\tau_{\text{ff}}}}{\tau_{\text{ff}}} \right), \quad (1)$$

where  $S_0$  is the flux density normalisation,  $\nu$  is the frequency in GHz,  $\nu_0 = 1$  GHz is the reference frequency,  $\eta$  is the absorption-free spectral index and  $\tau_{\text{ff}}$  is the free-free emission optical depth. Here, the last term in the bracket on the right-hand side of the equation denotes the escape probability of the photons; this expression can be obtained by solving the radiation transport equation using the large-scale velocity approximation under the assumption of spherical symmetry (de Jong et al. 1975). In the expression for the free-free Gaunt factor at radio wavelengths from Brusaard & van de Hulst (1962), the optical depth is given as

$$\tau_{\text{ff}} = 8.2 \times 10^{-2} \nu^{-2.1} T_e^{-1.35} \text{EM}, \quad (2)$$

with the emission measure (EM) in units of  $\text{cm}^{-6} \text{pc}$  and the electron temperature  $T_e$  in K. The EM is defined as

$$\left( \frac{\text{EM}}{\text{pc cm}^{-6}} \right) = \int_0^{s_0} \left( \frac{n_e}{\text{cm}^{-3}} \right)^2 \left( \frac{ds}{\text{pc}} \right), \quad (3)$$

where  $n_e$  is the thermal free electron density, and  $ds$  is the infinitesimal depth element along the line of sight between the source at  $s_0$  and an observer at 0. We combine Equations (2) and (1) to make a single free-free absorption fit model with three free parameters:  $S_0$ ,  $\eta$  and EM. The electron temperature is assumed to be  $T_e = 10^4$  K. The value of electron temperature does not affect the shape of the spectrum, only the resulting value of EM.

Alternatively, the free-free absorption could occur in the intervening region (essentially a screen), which is also likely to contain thermal gas, in particular since the H II regions are small compared to the thickness of the disk. Our data cannot distinguish between this external model and the internal model presented in Eq. (1), both of them fit the data and they look remarkably similar. We use the internal model as our fiducial model. In

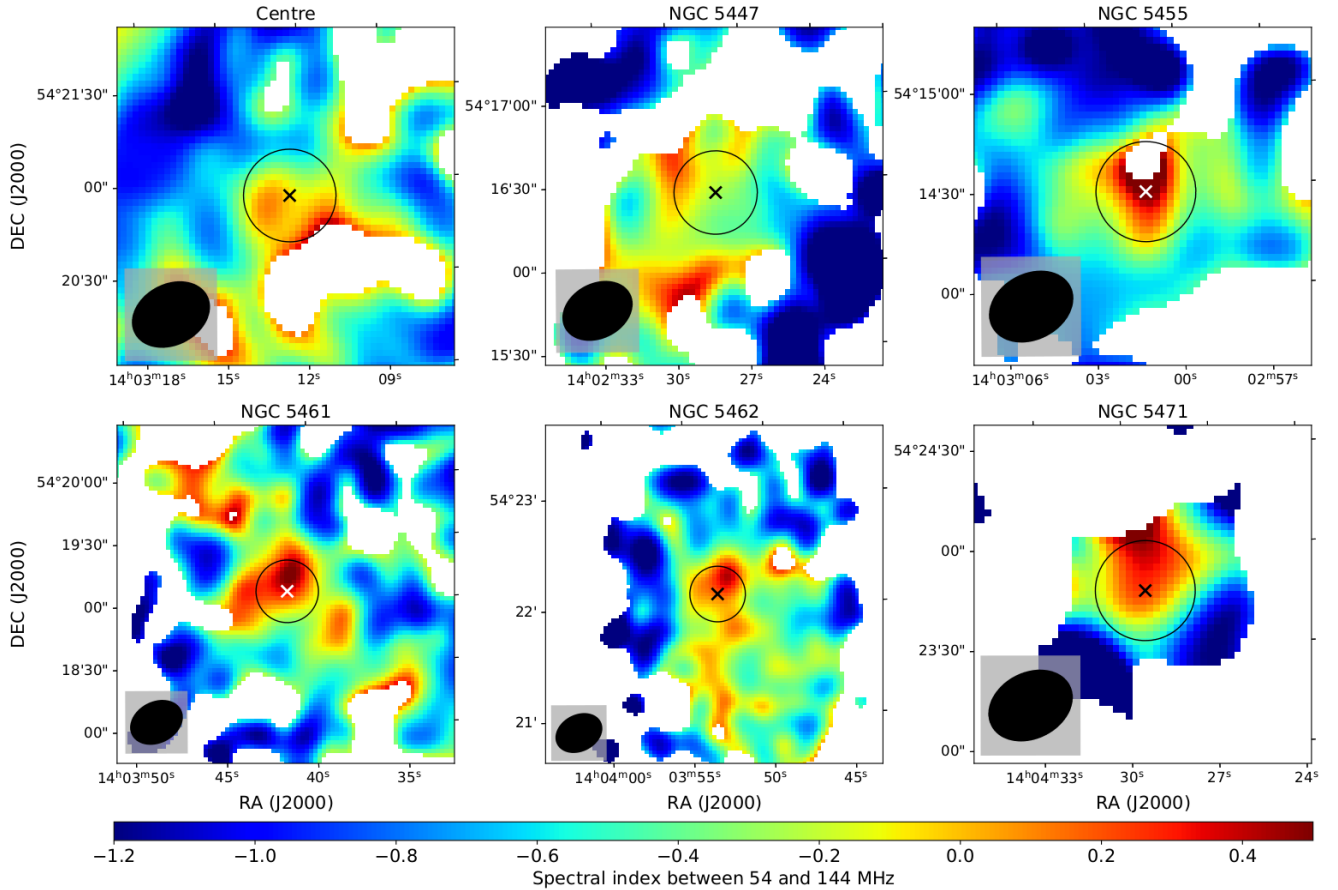


**Fig. 7.** Zoomed-in spectral index maps of H II regions in M 101 between 54 and 144 MHz. The regions where the spectrum is measured (in Sect. 4.2) are indicated with black circles and the centres of the regions (Table 3) are marked with an x. White areas below  $2\sigma$  are excluded. The beam size is shown with the black ellipse in the bottom left corner of each panel.

an external model, the spectrum no longer has the optical depth in the denominator, yielding (Wills et al. 1997)

$$S_\nu = S_0 \left( \frac{\nu}{\nu_0} \right)^\eta e^{-\tau_{\text{ff}}} \quad (4)$$

The external model leads to lower values of EM because all the absorption occurs in front of the source thus requiring less ionised gas. The fit results for both models are in Table 4.

In most of the analysed H II regions the flux density at 54 MHz is significantly lower than it would be if the power law behaviour extended to lower frequencies. The exception is the region NGC 5447 where the spectrum is entirely a power law with no absorption at low frequencies. We exclude this region from further collective analysis and analyse it separately in Sect. 5.3.

We observe a flattening in the spectrum of H II regions at frequencies below 100 MHz. Assuming  $T_e = 10^4$  K and the “internal” free-free absorption model we get values of the EM between 4800 and 12 000  $\text{cm}^{-6}$  pc. Fitting a different temperature does not change the fits because the parameter  $T_e^{-1.35} \cdot \text{EM}$  enters the fit (Eq. (2)). Hence changing  $T_e$  leads to a change in the inferred value of EM. Kennicutt et al. (2003) measured  $T_e$  for each of the H II regions and the values for  $T_e$  vary between 9000 K and 12 000 K for the low-ionisation zones. This would lead to a change in EM of 25% at most (which is less than other uncertainties). The initial values of EM are of the same order of magnitude but higher than the values determined for the spiral arms of M51 assuming that the flattening in the spectrum is

caused by free-free absorption (Gajović et al. 2024). In Sect. 5.1 we compare the values of EM obtained by fitting the low frequency radio absorption to a different tracer of EM.

The spectral indices of the H II regions are very close for both models. Their values are between  $-0.52$  and  $-0.22$  which is fairly flat. Thermal emission has a spectral index  $-0.1$  and non-thermal radio emission has a spectral index higher than  $-0.7$ . We observe a combination of thermal and non-thermal emission coming from the centres of H II regions.

We note that synchrotron self-absorption is not a viable explanation for the spectral behaviour as it requires brightness temperatures well in excess of the ones we measure (see Gajović et al. 2024 for an exact calculation). Moreover, ionisation losses of the cosmic-ray electrons do not lead to spectral down-turns but only to a flattening of spectra. Also, since H II regions are already ionised, ionisation losses should not play a major role.

## 5. Discussion

### 5.1. Comparison to other EM tracers

One can independently estimate the EM from the  $\text{H}\alpha$  flux density using the relation (Dettmar 1992; Voigtländer et al. 2013):

$$\text{EM} = 5 \cdot 10^{17} F_{\text{H}\alpha} / \Omega \quad (5)$$

where  $F_{\text{H}\alpha}$  is the  $\text{H}\alpha$  flux density in  $\text{erg cm}^{-2} \text{s}^{-1}$ , and  $\Omega$  is the collecting area in  $\text{arcsec}^2$  and EM is in  $\text{cm}^{-6}$  pc.



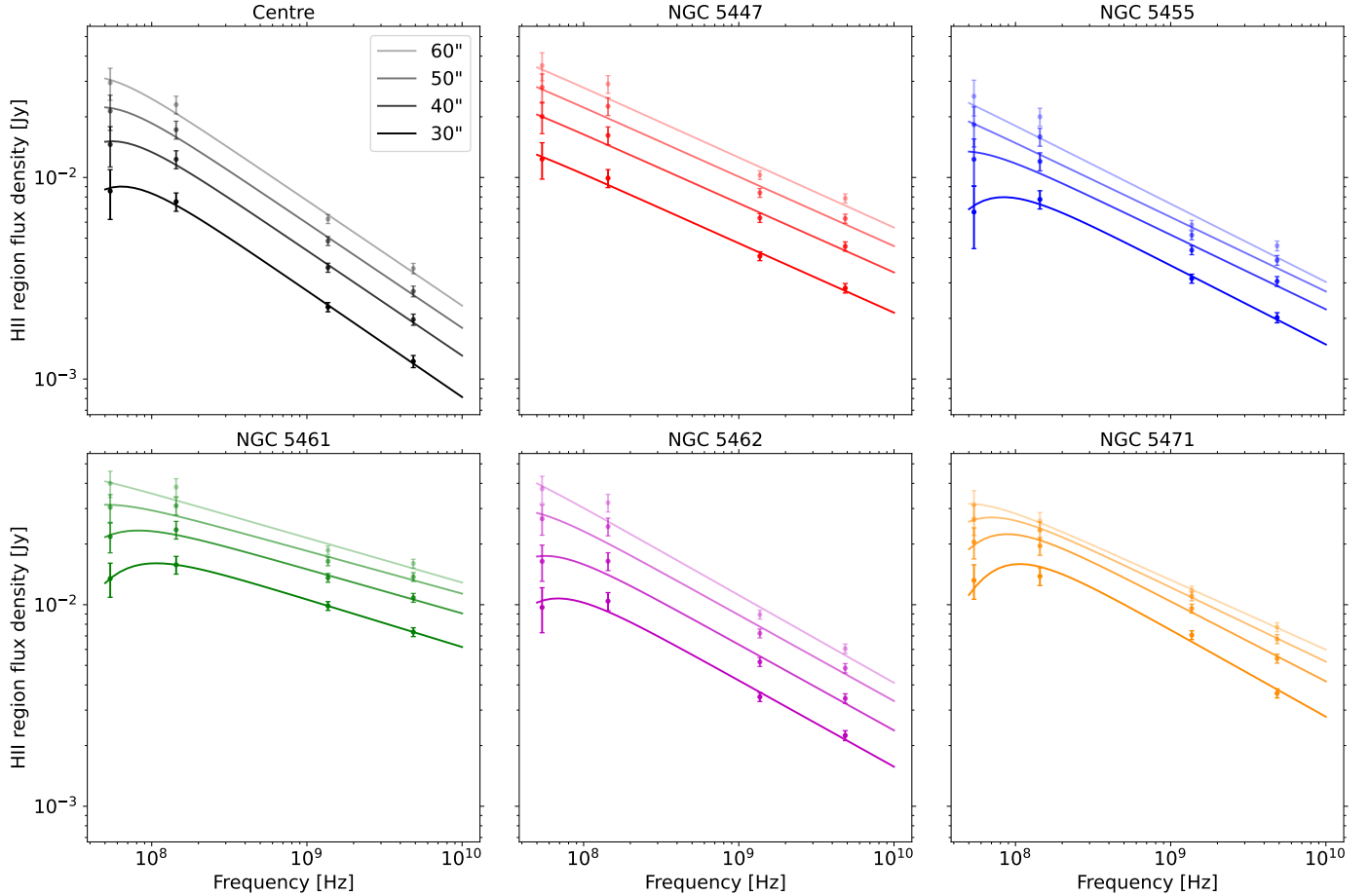


**Fig. 8.** Spectra of the selected H II regions in M 101. The solid lines of different opacity correspond to fits for the free–free absorption model (combined Eq. (1) and (2)) in different areas within which the flux is measured, with diameters from 30 to 60'' with a 10'' step. The fit parameters for the 30'' area are in Table 4.

**Table 4.** Fitted parameters for the spectra of the giant H II regions in M 101. The spectra are measured in areas with a 30'' diameter.

Region	Internal model		External model	
	$\eta$	EM [pc cm <sup>-6</sup> ]	$\eta$	EM [pc cm <sup>-6</sup> ]
Centre	$-0.528 \pm 0.044$	$5200 \pm 5200$	$-0.528 \pm 0.043$	$2500 \pm 2200$
NGC 5447	$-0.344 \pm 0.035$	$200 \pm 3300$	$-0.343 \pm 0.039$	$0 \pm 1800$
NGC 5455	$-0.393 \pm 0.041$	$6700 \pm 6100$	$-0.392 \pm 0.040$	$3200 \pm 2600$
NGC 5461	$-0.236 \pm 0.036$	$6600 \pm 4100$	$-0.235 \pm 0.035$	$3000 \pm 1700$
NGC 5462	$-0.428 \pm 0.041$	$4800 \pm 4600$	$-0.429 \pm 0.040$	$2300 \pm 2000$
NGC 5471	$-0.431 \pm 0.036$	$12300 \pm 5300$	$-0.424 \pm 0.034$	$4900 \pm 1800$

The  $H\alpha$  fluxes for our H II regions (except for the galactic centre) are presented in Hippelein (1986) who adapted them from Israel & Kennicutt (1980). The exact collecting areas for each region are not available, but their diameters range between 20'' and 40''. We assumed a diameter of 30'' for all our regions, because this diameter matches the regions in which we measured the radio flux and the range of possible diameters for the  $H\alpha$  measurements. The EM estimate using the  $H\alpha$  flux density as proxy is compared to the EM obtained by fitting the internal free–free absorption model to the radio data in Fig. 9. We exclude the galactic centre because of missing  $H\alpha$  data and NGC 5447 since we do not observe a turnover in that region.

The EM from radio and from  $H\alpha$  is the same order of magnitude, but the radio fits are consistently about two times higher

than the  $H\alpha$  estimates. Here we plot the EM from the internal free–free absorption model (Eq. (1)), however in Table 4 we show that the external model (Eq. (4)) results in consistently lower values of EM. The values from the external model are about a factor of two lower, which is more in line with the  $H\alpha$ . This is an indication that the external model could be more appropriate for the spectra of H II regions. However, due to the high uncertainty on the radio fit results and the unknown area for  $H\alpha$  measurements we cannot firmly claim which model is better.

## 5.2. Turnover localisation

The spectral index maps (Fig. 7) show inverted spectra right in the centres of the H II regions. In Fig. 8, it is clear that the

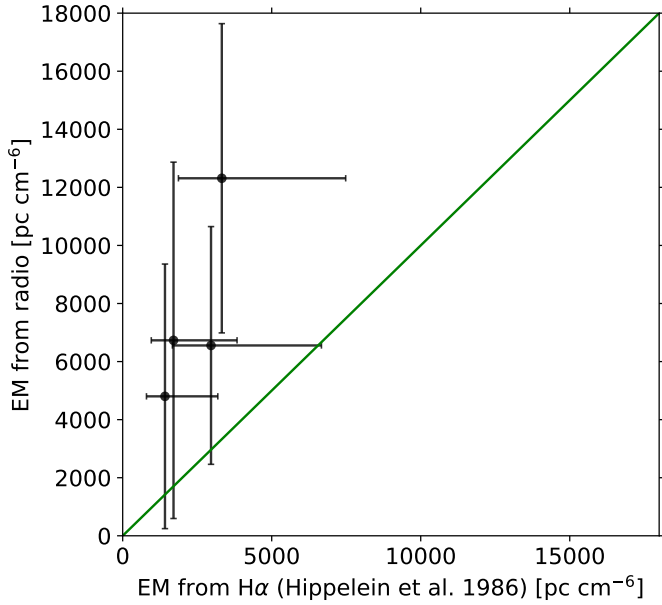


**Fig. 9.** Comparison of EM values from the internal free–free absorption model fit to the radio data and EM values from  $H\alpha$ . The 1:1 line is plotted in green.

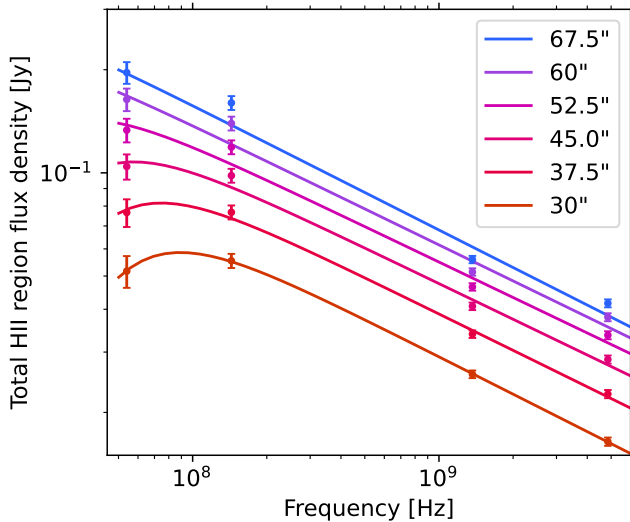


**Fig. 10.** Total flux density of H II regions measured in increasing areas around the centre of the region. NGC 5447 is excluded.

turnover can only be observed if we focus on a small area around the centre of the H II region. We now investigate how the size of the area affects our ability to observe a flattening in the spectrum. We added up the fluxes of the five selected H II regions (excluding NGC 5447) to create the total H II region spectrum. To get a more precise view, we varied the size of the area in which the flux density is measured between 30'' and 67.5'' in steps of 7.5''. In Fig. 10, we show how this affects the total H II region spectrum. We also fitted the free–free absorption model to those spectra. The fluxes of the H II regions are comparable so the total spectrum is not dominated by the brightest region.

From Fig. 10, we see that the low frequency flattening in the radio spectrum can not be detected if the area in which the flux density of the H II region is measured has a diameter larger than 45''. This corresponds to 1.5 kpc at the distance of M 101 (see

Table 1). This means that the flattening is only observable in the very centre of the H II region. With the increase of the area we include more of the surrounding part of the H II region and the flattening gets “diluted”.

It was already shown by Israel et al. (1975) that more than 50% (in some regions even up to 90%) of the radio flux density of the H II regions in M 101 is concentrated in the core. It is therefore not surprising that the free–free absorption is also most prominent in the cores, but it is interesting that the area where we detect the flattening has a diameter smaller than 1'.

This has important implications for future studies of H II regions at very low frequencies. To detect the low frequency flattening, the resolution of the radio maps has to be high enough that the centres of the H II regions with the flattening can be resolved from the surroundings. Our results on M 101 show that the beam size should be small enough to correspond to 1.5 kpc or less in the observed galaxy. M 101 has exceptionally bright and dense H II regions, so we expect that an even better resolution might be needed in other galaxies. The international baselines of the LOFAR telescope allow to reach a resolution around 1'' at 54 MHz (Groeneveld et al. 2022). If that is combined with SKA observations of similar resolution at higher frequency, in the future it could be possible to observe flattening in extragalactic H II regions at distances up to 300 Mpc.

### 5.3. NGC 5447 at low radio frequencies

NGC 5447 is the H II region in which we do not see a flattening at frequencies down to 54 MHz (top middle panel of Fig. 8). There are no known background radio sources that could affect the flux density in the location of NGC 5447. If we examine the spectral index of NGC 5447 (top middle panel of Fig. 7), we see that around the centre of the region the spectral index is not inverted. There are only two patches with an inverted spectrum near the edges of the H II region. It is probably the case that the area in which we measure the spectrum, does not include the parts of the region where there is a flattening. If we look at the  $H\alpha$  + continuum map of NGC 5447 (Fig. 11), it is revealed that this region consists of multiple distinct condensations, which can also be classified as separate H II regions. The area where we measure the spectrum in previous section is centred on the north-west condensation. We also try centring the area on the south-east condensation, but this does not change the result and we still do not detect a low frequency flattening. Our result can be explained if the free–free absorption only occurs in small condensations and our resolution is not sufficient to separate the emission with the turnover from the surroundings. This idea could be tested by higher resolution imaging using the international LOFAR stations. This region is also an exception in the work by Israel et al. (1975) because it is the only region in which they did not see a core component in 6 cm observations. With the perspective we get from our results, that could also be a consequence of the radio emission being produced by multiple distinct condensations and not one core.

Alternatively, different properties of NGC 5447 could be because of its position within M 101. It is located next to the big hole in the disk of M 101 that hosts only hot X-ray gas and potentially strong vertical magnetic fields, which could be a result of heating by magnetic reconnection (Weżgowiec et al. 2022). It is possible that the hole influenced the structure of NGC 5447. In addition to that, the H II regions on the East of the galaxy could be different from NGC 5447 because of the tidal interaction of M 101 with the galaxy to the east that also distorts the magnetic arm of M 101 (Weżgowiec et al. 2022).

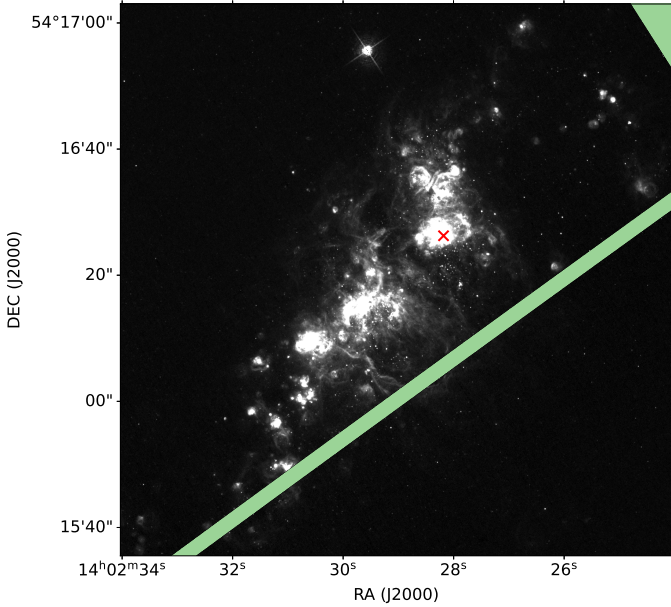


**Fig. 11.** NGC 5447 in  $H\alpha$  + continuum from the Hubble Legacy Archive<sup>1</sup>. The pale green area was not observed. The red x marks the centre of the area in which we measured the spectrum.

#### 5.4. Implication for spectral flattening and radio–FIR correlation

The nearly linear, tight correlation of far-infrared (FIR), and radio luminosity of star-forming galaxies is an important property to measure extinction-free star formation rates (Yun et al. 2001). This correlation can be explained if the cosmic ray electrons do not escape the galaxy in the so-called calorimetric model (Voelk 1989). However, in such a case the radio continuum spectra should be steep with integrated radio spectral indices around  $\alpha \approx -1.1$  (see e.g. Lacki et al. 2010). The integrated radio spectral index of galaxies is an important proxy for energy losses and transport effects of cosmic-ray electrons. Synchrotron and inverse Compton radiation losses tend to steepen the radio continuum spectrum, whereas Bremsstrahlung and ionisation losses tend to flatten the spectrum. With our new results we can now quantify the importance of other effects, namely of free–free absorption. The mean emission measure of our H II regions is  $(7000 \pm 2600) \text{ pc cm}^{-6}$  for the internal model. According to Equation (2) the optical depth is  $(2.3 \pm 0.8) \cdot 10^{-3}$  at 1 GHz and  $0.28 \pm 0.11$  at 100 MHz. This means that the decrement due to free–free absorption can be neglected at 1 GHz and is of order 30% at 100 MHz. We expect that integrated over the entire galaxy, these values are even smaller as the free–free absorption occurs only in regions with dense ionised gas. This means that in regular star forming galaxies, free–free absorption as a cause for spectral flattening may be neglected at frequencies  $\gtrsim 100$  MHz. Only in the nuclei of starburst galaxies may such an explanation be worthwhile as both observations (Adebahr et al. 2013) and simulations (Werhahn et al. 2021) suggest.

The observed flat radio spectral indices (Fig. 8, Table 4), flatter than the canonical injection spectral indices, hint at other

energy losses at work. Because they are not strongly frequency-dependent, we do not see a strong downturn at low frequencies. Also, the contribution of free–free emission will flatten the spectrum further at higher frequencies. A positive correlation between spectral curvature and neutral gas density was already found by Gajović et al. (2024) in M 51 corroborating the importance of low energy ionisation losses of the cosmic-ray electrons.

## 6. Conclusions

We present new radio continuum maps of M 101 at 54 and 1370 MHz. We study the giant H II regions at low radio frequencies. The centre of the galaxy and five giant H II regions (NGC 5447, NGC 5455, NGC 5461, NGC 5462, and NGC 5471) are selected for the analysis because they are bright at 144 MHz.

The spectral index between 54 and 144 MHz is negative in the very centres of the H II regions. The radio spectra of five out of six giant H II regions in M 101 show a flattening below 100 MHz. We do not see a turnover in the spectrum of NGC 5447, likely because it consists of several smaller condensations. The flattening observed in the majority of the selected regions can be well fitted with both the internal and external free–free absorption model and our data do not show preference for either model. The resulting EMs are about a factor of two lower for the external model and that is more in line with the EMs estimated from  $H\alpha$  fluxes. This is an indication that the external free–free absorption model is better for H II regions, but because of high uncertainties it is only an indication.

Low-frequency flattening is only present in the very centre of the giant H II regions. The area where radio spectrum is measured has to be smaller than 1.5 kpc (corresponds to  $45''$  in M 101) to detect a flattening. In the future, to detect the low frequency flattening in more distant H II regions, high resolution observations will have to be performed with the SKA and LOFAR international stations.

Our findings indicate that free–free absorption at frequencies around 100 MHz has an optical depth of  $\approx 0.3$  (Sect. 5.4). This means free–free absorption has to be taken into account when observing H II regions. Globally, however, the effect of free–free absorption is much smaller. This has important consequences when using radio continuum observations to measure extinction-free star-formation rates on kiloparsec scales at frequencies of  $\lesssim 100$  MHz (e.g. Heesen et al. 2019).

*Acknowledgements.* We thank the anonymous referee for their comments, which helped to strengthen the conclusions of the paper. We thank M. Weigowicz for providing the FITS files for the 4850 MHz maps. LG and MB acknowledge funding by the Deutsche Forschungsgemeinschaft (DFG, German Research Foundation) under Germany’s Excellence Strategy – EXC 2121 “Quantum Universe” – 390833306. BA and DJB acknowledge funding from the German Science Foundation DFG, via the Collaborative Research Center SFB1491 ‘Cosmic Interacting Matters – From Source to Signal’. FdG acknowledges support from the ERC Consolidator Grant ULU 101086378. LOFAR (van Haarlem et al. 2013) is the Low Frequency Array designed and constructed by ASTRON. It has observing, data processing, and data storage facilities in several countries, which are owned by various parties (each with their own funding sources), and that are collectively operated by the ILT foundation under a joint scientific policy. The ILT resources have benefited from the following recent major funding sources: CNRS-INSU, Observatoire de Paris and Université d’Orléans, France; BMBF, MIWF-NRW, MPG, Germany; Science Foundation Ireland (SFI), Department of Business, Enterprise and Innovation (DBEI), Ireland; NWO, The Netherlands; The Science and Technology Facilities Council, UK; Ministry of Science and Higher Education, Poland; The Istituto Nazionale di Astrofisica (INAF), Italy. This research made use of the Dutch national e-infrastructure with support of the SURF Cooperative (e-infra 180169) and the LOFAR e-infra group. The Jülich LOFAR Long Term Archive and the German LOFAR network are both coordinated and operated by the Jülich Supercomputing Centre (JSC), and computing resources on the supercomputer JUWELS at JSC were provided by the Gauss Centre for Supercomputing e.V. (grant

<sup>1</sup> Based on observations made with the NASA/ESA Hubble Space Telescope, and obtained from the Hubble Legacy Archive, which is a collaboration between the Space Telescope Science Institute (STScI/NASA), the Space Telescope European Coordinating Facility (ST-ECF/ESA) and the Canadian Astronomy Data Centre (CADCA/NRC/CSA).

CHTB00) through the John von Neumann Institute for Computing (NIC). This research made use of the University of Hertfordshire high-performance computing facility and the LOFAR-UK computing facility located at the University of Hertfordshire and supported by STFC [ST/P000096/1], and of the Italian LOFAR IT computing infrastructure supported and operated by INAF, and by the Physics Department of Turin university (under an agreement with Consorzio Interuniversitario per la Fisica Spaziale) at the C3S Supercomputing Centre, Italy. The research leading to these results has received funding from the European Research Council under the European Union's Seventh Framework Programme (FP/2007–2013) / ERC Advanced Grant RADIOLIFE-320745. This research made use of the Python Kapteyn Package (Terlouw & Vogelaar 2015). Partly based on observations made with the NASA/ESA Hubble Space Telescope, and obtained from the Hubble Legacy Archive, which is a collaboration between the Space Telescope Science Institute (STScI/NASA), the Space Telescope European Coordinating Facility (ST-ECF/ESA) and the Canadian Astronomy Data Centre (CAD/C/NRC/CSA).

## References

- Adams, E. A., Adebahr, B., Connor, L., et al. 2020, *Am. Astron. Soc. Meet. Abstr.*, **235**, 136.07
- Adebahr, B., Krause, M., Klein, U., et al. 2013, *A&A*, **555**, A23
- Adebahr, B., Krause, M., Klein, U., Heald, G., & Dettmar, R. J. 2017, *A&A*, **608**, A29
- Anantharamaiah, K. R., Viallefond, F., Mohan, N. R., Goss, W. M., & Zhao, J. H. 2000, *ApJ*, **537**, 613
- Basu, A., Mitra, D., Wadadekar, Y., & Ishwara-Chandra, C. H. 2012, *MNRAS*, **419**, 1136
- Basu, A., Roychowdhury, S., Heesen, V., et al. 2017, *MNRAS*, **471**, 337
- Berkhuijsen, E. M., Urbanik, M., Beck, R., & Han, J. L. 2016, *A&A*, **588**, A114
- Brown, L. W. 1973, *ApJ*, **180**, 359
- Brussaard, P. J., & van de Hulst, H. C. 1962, *Rev. Mod. Phys.*, **34**, 507
- Caprioli, D., Amato, E., & Blasi, P. 2010, *Astropart. Phys.*, **33**, 307
- Caswell, J. L., & Wills, D. 1967, *MNRAS*, **135**, 231
- Chyży, K. T., Jurusik, W., Piotrowska, J., et al. 2018, *A&A*, **619**, A36
- Condon, J. J., Cotton, W. D., & Broderick, J. J. 2002, *AJ*, **124**, 675
- Conway, J. E., Elitzur, M., & Parra, R. 2018, *ApJ*, **865**, 70
- Corwin, H. G. 1995, *NED Team Report*, **1**, 1
- de Gasperin, F., Dijkema, T. J., Drabent, A., et al. 2019, *A&A*, **622**, A5
- de Gasperin, F., Williams, W. L., Best, P., et al. 2021, *A&A*, **648**, A104
- de Gasperin, F., Edler, H. W., Williams, W. L., et al. 2023, *A&A*, **673**, A165
- de Jong, M. L. 1965, *ApJ*, **142**, 1333
- de Jong, T., Chu, S., & Dalgarno, A. 1975, *ApJ*, **199**, 69
- de La Beaujardière, O., Kazés, I., Le Squeren, A. M., & Nguyen-Quang-Rieu, 1968, *Ann. Astrophys.*, **31**, 387
- de Vaucouleurs, G., de Vaucouleurs, A., Corwin, H. G., Jr., et al. 1991, *Third Reference Catalogue of Bright Galaxies* (New York, NY: Springer)
- Dénes, H., Hess, K. M., Adams, E. A. K., et al. 2022, *A&A*, **667**, A40
- Dettmar, R. J. 1992, *Fund. Cosmic Phys.*, **15**, 143
- Dodorico, S., Rosa, M., & Wampler, E. J. 1983, *A&AS*, **53**, 97
- Gajović, L., Adebahr, B., Basu, A., et al. 2024, *A&A*, **689**, A68
- Gioia, I. M., Gregorini, L., & Klein, U. 1982, *A&A*, **116**, 164
- Gordon, K. D., Engelbracht, C. W., Rieke, G. H., et al. 2008, *ApJ*, **682**, 336
- Graeve, R., Klein, U., & Wielebinski, R. 1990, *A&A*, **238**, 39
- Green, D. A. 2014, *Bull. Astron. Soc. India*, **42**, 47
- Groeneveld, C., van Weeren, R. J., Miley, G. K., et al. 2022, *A&A*, **658**, A9
- Heesen, V., Buie, E., I., Huff, C. J., et al. 2019, *A&A*, **622**, A8
- Heesen, V., Staffehl, M., Basu, A., et al. 2022, *A&A*, **664**, A83
- Hippelein, H. H. 1986, *A&A*, **160**, 374
- Hiramatsu, D., Tsuna, D., Berger, E., et al. 2023, *ApJ*, **955**, L8
- Hodge, P. W. 1969, *ApJS*, **18**, 73
- Hodge, P. W., Gurwell, M., Goldader, J. D., & Kennicutt, R. C., Jr. 1990, *ApJS*, **73**, 661
- Hoopes, C. G., Walterbos, R. A. M., & Bothun, G. D. 2001, *ApJ*, **559**, 878
- Hu, N., Wang, E., Lin, Z., et al. 2018, *ApJ*, **854**, 68
- Hummel, E. 1991, *A&A*, **251**, 442
- Ignesti, A., Vulcani, B., Poggianti, B. M., et al. 2022, *ApJ*, **924**, 64
- Israel, F. P., & Kennicutt, R. C. 1980, *Astrophys. Lett.*, **21**, 1
- Israel, F. P., & Mahoney, M. J. 1990, *ApJ*, **352**, 30
- Israel, F. P., Goss, W. M., & Allen, R. J. 1975, *A&A*, **40**, 421
- Kapińska, A. D., Staveley-Smith, L., Crocker, R., et al. 2017, *ApJ*, **838**, 68
- Kennicutt, R. C., Jr., Bresolin, F., & Garnett, D. R. 2003, *ApJ*, **591**, 801
- Klein, U., Wielebinski, R., & Morsi, H. W. 1988, *A&A*, **190**, 41
- Klein, U., Lisenfeld, U., & Verley, S. 2018, *A&A*, **611**, A55
- Konar, C., Hardcastle, M. J., Jamroz, M., & Croston, J. H. 2013, *MNRAS*, **430**, 2137
- Kuril'Chik, V. N. 1966, *Soviet Ast.*, **10**, 1
- Kutkin, A. M., Oosterloo, T. A., Morganti, R., et al. 2023, *A&A*, **676**, A37
- Lacki, B. C. 2014, *MNRAS*, **444**, L39
- Lacki, B. C., Thompson, T. A., & Quataert, E. 2010, *ApJ*, **717**, 1
- Lal, D. V., Lyskova, N., Zhang, C., et al. 2022, *ApJ*, **934**, 170
- Li, J.-T., Beck, R., Dettmar, R.-J., et al. 2016, *MNRAS*, **456**, 1723
- Marvil, J., Owen, F., & Eilek, J. 2015, *AJ*, **149**, 32
- Niklas, S., Klein, U., & Wielebinski, R. 1997, *A&A*, **322**, 19
- Oosterloo, T. A., Vedantham, H. K., Kutkin, A. M., et al. 2020, *A&A*, **641**, L4
- Pasini, T., Edler, H. W., Brügger, M., et al. 2022, *A&A*, **663**, A105
- Pohl, M., & Schlickeiser, R. 1990, *A&A*, **239**, 424
- Pohl, M., Schlickeiser, R., & Hummel, E. 1991a, *A&A*, **250**, 302
- Pohl, M., Schlickeiser, R., & Lesch, H. 1991b, *A&A*, **252**, 493
- Ramírez-Olivencia, N., Varenus, E., Pérez-Torres, M., et al. 2022, *A&A*, **658**, A4
- Roberts, I. D., van Weeren, R. J., Lal, D. V., et al. 2024, *A&A*, **683**, A11
- Rogstad, D. H., & Shostak, G. S. 1971, *A&A*, **13**, 99
- Roy, S., & Pramesh Rao, A. 2006, *J. Phys. Conf. Ser.*, **54**, 156
- Sault, R. J., Teuben, P. J., & Wright, M. C. H. 1995, in *Astronomical Data Analysis Software and Systems IV*, eds. R. A. Shaw, H. E. Payne, & J. J. E. Hayes, *ASP Conf. Ser.*, **77**, 433
- Shimwell, T. W., Hardcastle, M. J., Tasse, C., et al. 2022, *A&A*, **659**, A1
- Skillman, E. D., & Israel, F. P. 1988, *A&A*, **203**, 226
- Stein, M., Heesen, V., Dettmar, R. J., et al. 2023, *A&A*, **670**, A158
- Tabatabaei, F. S., Schinnerer, E., Krause, M., et al. 2017, *ApJ*, **836**, 185
- Tasse, C., Hugo, B., Mirmont, M., et al. 2018, *A&A*, **611**, A87
- Terlouw, J. P., & Vogelaar, M. G. R. 2015, *Kapteyn Package, Version 2.3* (Groningen: Kapteyn Astronomical Institute), Available from <http://www.astro.rug.nl/software/kapteyn/>
- Tingay, S. J., & de Kool, M. 2003, *AJ*, **126**, 723
- van Haarlem, M. P., Wise, M. W., Gunst, A. W., et al. 2013, *A&A*, **556**, A2
- van Weeren, R. J., Williams, W. L., Hardcastle, M. J., et al. 2016, *ApJS*, **223**, 2
- Varenus, E., Conway, J. E., Martí-Vidal, I., et al. 2016, *A&A*, **593**, A86
- Voelk, H. J. 1989, *A&A*, **218**, 67
- Voigtländer, P., Kamphuis, P., Marcelin, M., Bomans, D. J., & Dettmar, R. J. 2013, *A&A*, **554**, A133
- Vorontsov-Vel'Yaminov, B. A., & Arkhipova, V. P. 1962, *MCG*, **C01**, 0
- Werhahn, M., Pfrommer, C., & Girichidis, P. 2021, *MNRAS*, **508**, 4072
- Weżgowiec, M., Beck, R., Hanasz, M., et al. 2022, *A&A*, **664**, A108
- White, R. L., & Becker, R. H. 1992, *ApJS*, **79**, 331
- Wills, K. A., Pedlar, A., Muxlow, T. W. B., & Wilkinson, P. N. 1997, *MNRAS*, **291**, 517
- Yun, M. S., Reddy, N. A., & Condon, J. J. 2001, *ApJ*, **554**, 803

## Appendix A: Mask for the integrated spectrum

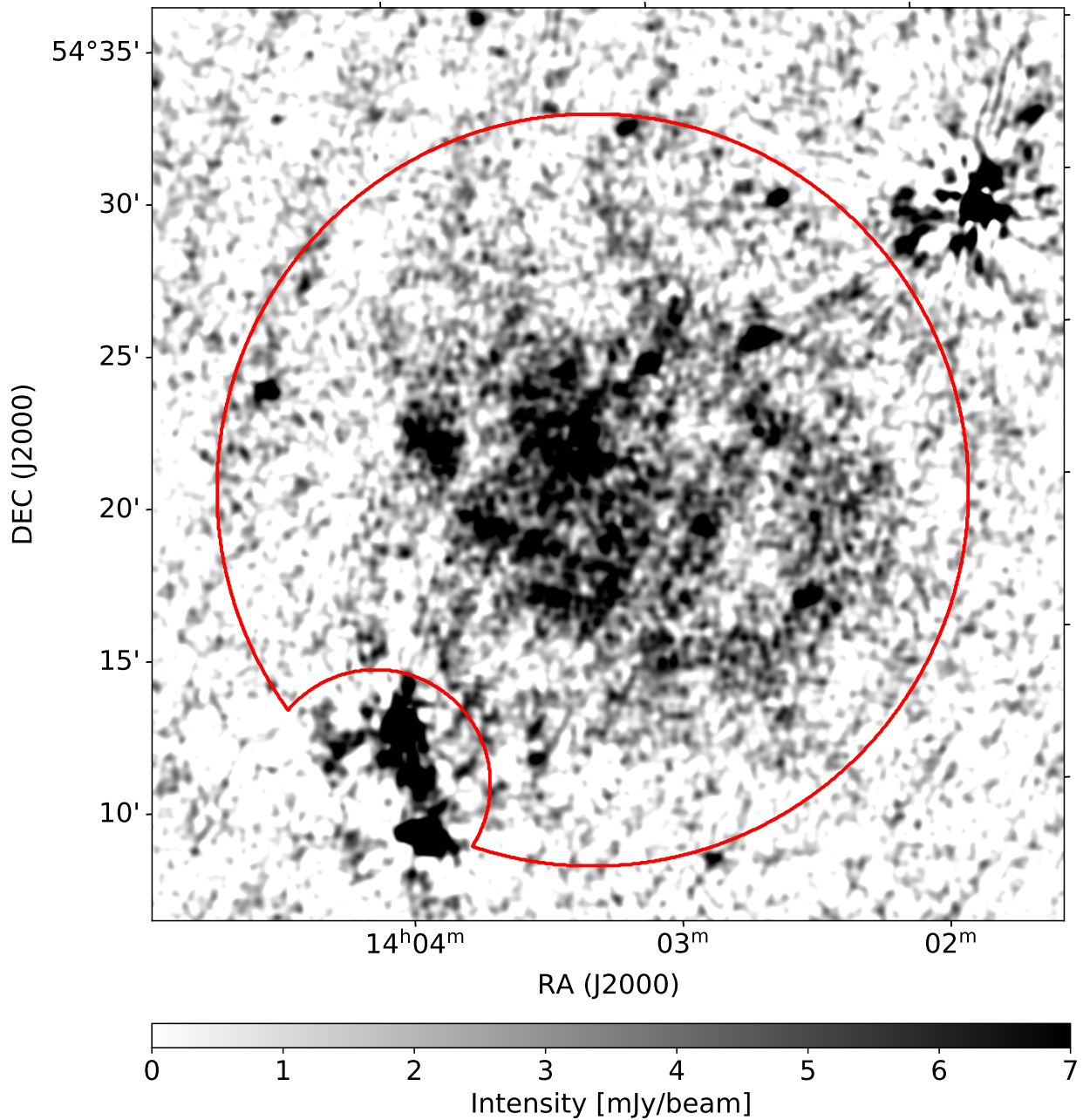


**Fig. A.1.** The region in which we calculated the integrated spectrum of M101. The region is plotted in red on top of the 54 MHz LBA map. The artefacts around background sources are most prominent in the LBA map so we use that map to make sure the artefacts are excluded.

## Appendix B: Archival integrated flux density measurements for M 101

Table B.1. Integrated flux density of M 101 from the literature and our observations.

Frequency [MHz]	Flux density [Jy]	Instrument type	Background sources removed	Beam size	Reference
54 <sup>(a)</sup>	5.02 ± 0.51	Interferometer	+	26'5 × 20''	1
57	6.5 ± 2.5	Interferometer	-	7' × 6'	2
144 <sup>(a)</sup>	3.18 ± 0.32	Interferometer	+	26'5 × 20''	3
178	2.4 ± 0.5	Interferometer	-	23' × 18'	4
610	1.4 ± 0.1	Interferometer	+	1' × 1'12''	5
750	1.3 ± 0.3	Single dish	-	18'30'' × 18'30''	6
920	1.3 ± 0.2	Transit	-	~ 8' in E-W direction	7
1370 <sup>(a)</sup>	0.537 ± 0.027	Interferometer	+	15'1 × 11'0	1
1400	0.75 ± 0.04	Interferometer	-	45'' × 45''	8
1400	0.81 ± 0.10	Single dish	-	11'40'' × 11'40''	9
1400	0.8 ± 0.1	Interferometer	-	4' × 4'	10
1410	0.82 ± 0.21	Single dish	-	10' × 10'	6
1415	0.85 ± 0.13	Interferometer	-	4' × 30'	11
2700	0.52 ± 0.06	Single dish	+	~ 4'30'' × 4'30''	12
2700	0.48 ± 0.03	Single dish	+	4'24'' × 4'24''	13
4750	0.335 ± 0.020	Single dish	+	2'27'' × 2'27''	12
4850	0.31 ± 0.02	Single dish	+	2'30'' × 2'30''	13
4850 <sup>(a)</sup>	0.308 ± 0.015	Combined	+	30'' × 30''	14
10700	0.207 ± 0.020	Single dish	+	1'30'' × 1'30''	12

**References.** (1) This paper; (2) Israel & Mahoney (1990); (3) Shimwell et al. (2022); (4) Caswell & Wills (1967); (5) Israel et al. (1975); (6) de Jong (1965); (7) Kuril'Chik (1966); (8) Condon et al. (2002); (9) White & Becker (1992); (10) Rogstad & Shostak (1971); (11) de La Beaujardière et al. (1968); (12) Graeve et al. (1990); (13) Berkhuijsen et al. (2016); (14) Weżgowiec et al. (2022);

<sup>(a)</sup>Map used in this work.

## Appendix C: Spectral index error map

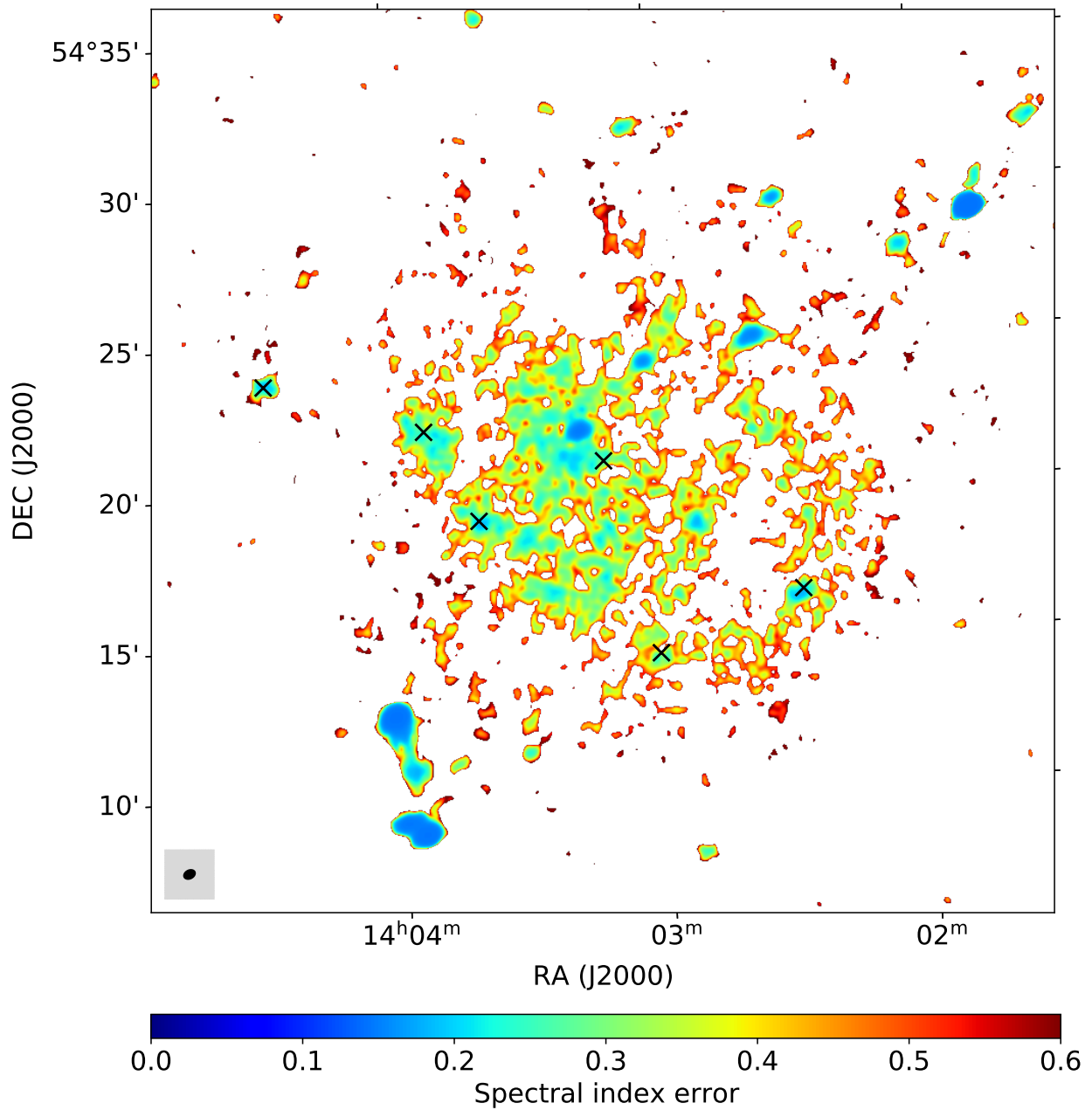


**Fig. C.1.** Spectral index error map between 54 MHz and 144 MHz. White areas below below  $2\sigma$  are excluded. The beam size is shown with the black ellipse in the bottom left corner. The centres of the studied H II regions are marked with an x to make them easier to find.